atmosphere

MDPI

Article

Assessing Earthquake Forecasting Performance Based on Annual Mobile Geomagnetic Observations in Southwest China

Zhe Ni [1], Hongyan Chen [2,*], Rui Wang [2], Miao Miao [2], Hengxin Ren [2], Jiehao Yuan [3], Zhendong Wang [3], Yufei Zhao [1] and Siyuan Zhou [1]

[1] Yunnan Earthquake Agency, Kunming 650224, China; nizhe2012@pku.org.cn (Z.N.); zyf202310@163.com (Y.Z.); zhousiyuan12151215@163.com (S.Z.)
[2] Department of Earth and Space Sciences, Southern University of Science and Technology, Shenzhen 518055, China; wangr9@sustech.edu.cn (R.W.); miaom@sustech.edu.cn (M.M.); renhx@sustech.edu.cn (H.R.)
[3] Institute of Geophysics, China Earthquake Administration, Beijing 100081, China; yuanjiehao@cea-igp.ac.cn (J.Y.); wangzd0626@sina.cn (Z.W.)
* Correspondence: chenhy@sustech.edu.cn; Tel.: +86-755-8801-5515

Abstract: There have been reports about anomalies in mobile geomagnetic data before earthquakes; however, whether it can be used as an indicator for identifying potential earthquake areas was not be explored. In this study, we propose two parameters for earthquake forecasting based on annual mobile geomagnetic observation data. The spatial horizontal and three components' changes are calculated in each year and then used to forecast moderate–large earthquakes ($M \geq 5.0$) in southwest China in the subsequent period. It is found that earthquakes are more likely to occur in low *H*- or *F*-value regions. We statistically assess their forecasting performance by using Molchan's error diagram, and the results indicate that there is considerable precursory information in the spatial *H* and *F* values. It is concluded that mobile geomagnetic observations might be useful in middle-term earthquake forecasts in the study area. We discuss the physical mechanisms of *H* and *F* values to explain their reasonability. The methodology proposed in this study could be helpful in finding out the optimal solution for annual mobile geomagnetic measurements for middle-term earthquake forecasting.

Keywords: mobile geomagnetic observation; earthquake forecasting performance; Molchan's error diagram; southwest China

Citation: Ni, Z.; Chen, H.; Wang, R.; Miao, M.; Ren, H.; Yuan, J.; Wang, Z.; Zhao, Y.; Zhou, S. Assessing Earthquake Forecasting Performance Based on Annual Mobile Geomagnetic Observations in Southwest China. *Atmosphere* **2023**, *14*, 1750. https://doi.org/10.3390/atmos14121750

Academic Editor: Sergey Pulinets

Received: 19 October 2023
Revised: 17 November 2023
Accepted: 26 November 2023
Published: 28 November 2023

1. Introduction

The eastern edge of the Qinghai-Tibet Plateau is one of the most seismically active regions on the Chinese mainland. According to the recorded earthquake catalog, in the past decades, it has experienced several strong earthquakes, including the M8.0 Wenchuan earthquake in 2008, the M7.0 Lushan earthquake in 2013, and the M7.0 Jiuzhaigou earthquake in 2017. The analysis of potential earthquake hazard zones is typically based on seismic activity [1–7]. However, for earthquake forecasting, especially middle- and short-term forecasting, only using earthquake catalog information is still far from enough, so scientists will often use other physical parameters, such as deformation, etc. [8–13]. In recent years, the geomagnetic field changes related to earthquakes, named seismo-geomagnetic phenomena, have been extensively studied [14–18]. Geomagnetic observations can be used as an auxiliary method for monitoring earthquake hazard zones, because they can reflect subsurface structures and abnormal activity [19–22].

Field studies show that various seismo-geomagnetic signals can be generated at the different stages of earthquake formation and occurrence [18,23–25]. These include the mid- and long-term resistivity changes before the earthquake [26–28], mid- and

short-term ultra-low-frequency (ULF) [14,29–33] and very low frequency (VLF) geomagnetic field changes [34–37], and changes in the total electron content (TEC) over a short period of hours/minutes [38–41]. Annual mobile geomagnetic observation is one of the observed methods for the geomagnetic field, which carries out periodic and repeated mobile observations on many geomagnetic observation sites in a specific area. The variation in a local magnetic field in the lithosphere can be obtained via mobile geomagnetic observation, which may contain the disturbance information of the underground stress field [42]. However, whether it can be used as an indicator for identifying forthcoming earthquake areas is debatable, and the forecasting performance has not been statistically tested yet. Therefore, this paper will utilize annual mobile geomagnetic observation data to assess earthquake forecasting performance in southwest China. The study area covers Yunnan Province, most of Sichuan Province, and part of southern Gansu Province.

2. Materials and Methods

2.1. Mobile Geomagnetic Data

The period of geomagnetic data in this paper is from 2010 to 2015. Mobile geomagnetic observations were conducted in the study area from March to June each year. The number of observation sites was 216 in 2010, 221 in 2011, and 235 from 2012 to 2015. The average distance between two adjacent observation sites was about 70 km, and the magnetic field environment around a single measuring site must be less than 5 nT/m within a radius of 5 m from the measuring site. The absolute values of total intensity, magnetic declination, and magnetic inclination were independently measured at each observation site. The total intensity of the geomagnetic field was measured using a proton precession magnetometer (GSM-19T) [43,44] with an absolute accuracy of $\pm$0.2 nT and a resolution of 0.01 nT. A magnetometer (CTM-DI) [45] with an accuracy of 0.20 and a resolution of 0.10 was used to measure the magnetic azimuth and inclination. The GPS instrument was used to measure the geographical azimuth of the measuring site, as well as the longitude, latitude, and elevation. The magnetic declination is calculated through the observation of magnetic azimuth and geographical azimuth. The other three components used, namely, the east component (Y), north component (X), and vertical component (Z), can be calculated through the above parameters.

2.2. Data Preprocessing Methods

The lithospheric magnetic field is obtained after eliminating the diurnal variation from the external field, the main magnetic field, and its long-term variation. Then, the annual variation in the lithospheric magnetic field is obtained by the difference of the adjacent two years' lithospheric magnetic field data. Thus, geomagnetic anomalies associated with earthquakes are captured during this change. The specific process of calculating the above data is divided into four steps:

1. First, diurnal correction is performed. This step is to eliminate the external field effect such as the diurnal variations. The single reference method is adopted, that is, the daily variation in observation data is corrected by the continuous observation of the geomagnetic station nearest to the measuring site. The diurnal variation correction day is selected as the relatively calm day in terms of the magnetic situation change during the month, and the time is from 0:00 to 3:00 (Beijing time). Five geomagnetic stations are selected within the study area: Lanzhou, Tianshui, Chengdu, Xichang, and Tonghai station. After performing the diurnal variation correction, the mean square error of the total intensity is less than 1.5 nT, and the mean square error of declination and inclination are less than 0.5 nT for all observation stations.
2. Second, long-term variation correction is carried out. This step is to eliminate secular variations from the main magnetic field in mobile geomagnetic observation data. Based on the 6-order NOC nonlinear model of secular variations for the geomagnetic

basic field [46–49] in China from 1995 to 2020, we obtain the secular variations for each observation in every year and correct their variation values.

3. Third, we eliminate the main magnetic field. This step is to eliminate the main magnetic field in the secular variation data using IGRF-12 as the main magnetic field reference model, which was published by the International Association of Geomagnetism and Aeronomy (IAGA) [50]. We calculate the differences between all secular correction data and IGRF-12 to obtain the lithospheric magnetic field data for each year from 2010 to 2015.
4. Finally, we calculate annual changes in the lithospheric magnetic field. This step is to obtain the annual changes in the lithospheric magnetic field by computing the differences in lithospheric magnetic field data in the adjacent two years.

2.3. H Value and F Value Calculation

Previous studies found anomalous characteristics before earthquakes in X, Y, and Z components [51–53]. Therefore, the analysis data in this article adopt the horizontal or three-component changes in the lithospheric magnetic field. We divide the study area into 0.1° grid for analysis. We calculate the mean magnitude of resultant vector for horizontal or three-component changes for stations, and we abbreviate them to *H* value or *F* value, respectively. The *H* value is calculated as follows:

$$H = \frac{|\overrightarrow{\delta_{H_1}} + \overrightarrow{\delta_{H_2}} + \cdots + \overrightarrow{\delta_{H_m}}|}{m} \tag{1}$$

where m is the number of stations in a certain radius around a grid point, $\overrightarrow{\delta_{H_m}}$ is the horizontal component (X and Y) change for the m'th station, and $|\overrightarrow{\delta_{H_1}} + \overrightarrow{\delta_{H_2}} + \cdots + \overrightarrow{\delta_{H_m}}|$ is the magnitude of resultant vector of horizontal component change for these m stations. In addition, we define *F* value as follows:

$$F = \frac{|\overrightarrow{\delta_{F_1}} + \overrightarrow{\delta_{F_2}} + \cdots + \overrightarrow{\delta_{F_m}}|}{m} \tag{2}$$

where m is the number of stations in a certain radius around a grid point, $\overrightarrow{\delta_{F_m}}$ is the three-component (X, Y and Z) change for the m'th station, and $|\overrightarrow{\delta_{F_1}} + \overrightarrow{\delta_{F_2}} + \cdots + \overrightarrow{\delta_{F_m}}|$ is the magnitude of resultant vector of three-component change for these stations. An additional description for abbreviations and symbols is designed in Appendix A. The study area and the mobile magnetic observation sites (in 2011 and 2012 as example) are shown below in Figure 1. In practice, it takes time to preprocess and analyze the data after data collection in June, so we assess the earthquake forecasting performance in the subsequent period from August of the current year to July of the next year.

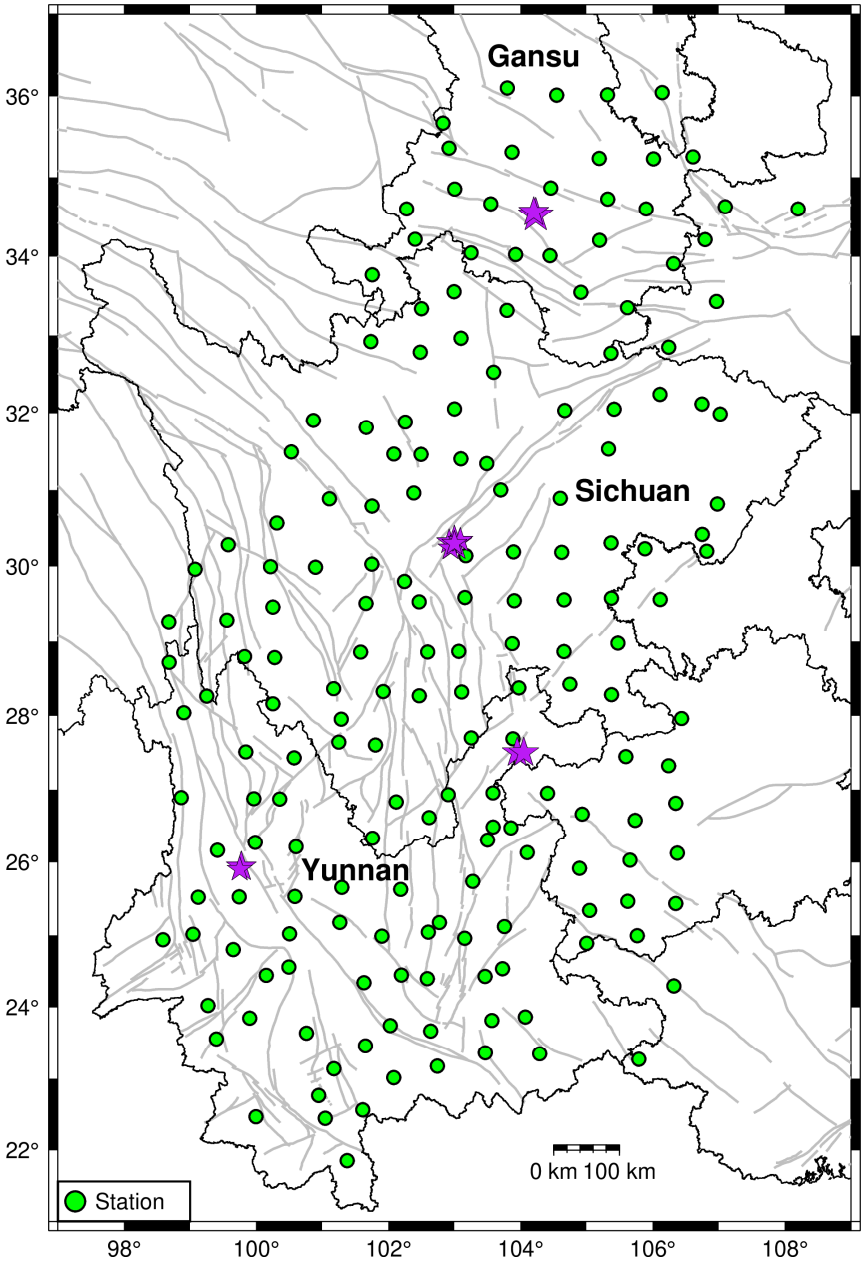

Figure 1. The spatial distribution of mobile geomagnetic observations in the study area of 2011 and 2012. The black lines are the provincial boundaries. The gray lines indicate main faults. The purple stars show locations of earthquake events with M $\geq$ 5.0 during August 2012–July 2013. The size of the symbol is scaled to the magnitude.

3. Results

3.1. Spatial H Value and F Value in Each Year

The *H* value and *F* value calculation is applied to the earthquake catalog with M $\geq$ 5.0 in each year in the study area. The results of the spatial *H* values and *F* values during June 2010–June 2011, June 2011–June 2012, June 2012–June 2013, June 2013–June 2014, and June 2014–June 2015 are shown in Figures 2–6, respectively. The moderate–large earthquakes in the subsequent period are also plotted for analyses. The earthquakes are the M $\geq$ 5.0 catalog during August 2011–July 2012, August 2012–July 2013, August 2013–July 2014, August 2014–July 2015, and August 2015–July 2016, respectively. We calculate *H* and *F* values in those grid points where the number of stations (Num) $\geq$ 3 within a 100 km radius, so there are no values in some grid points for the sparsely measured area. It should be

noted that we can only analyze earthquakes with H and F values at the grid points, so earthquakes without H or F values at the grid point are not listed (four earthquakes totally in five years). The detailed earthquake information for analyses in this paper is listed in Tables 1–5.

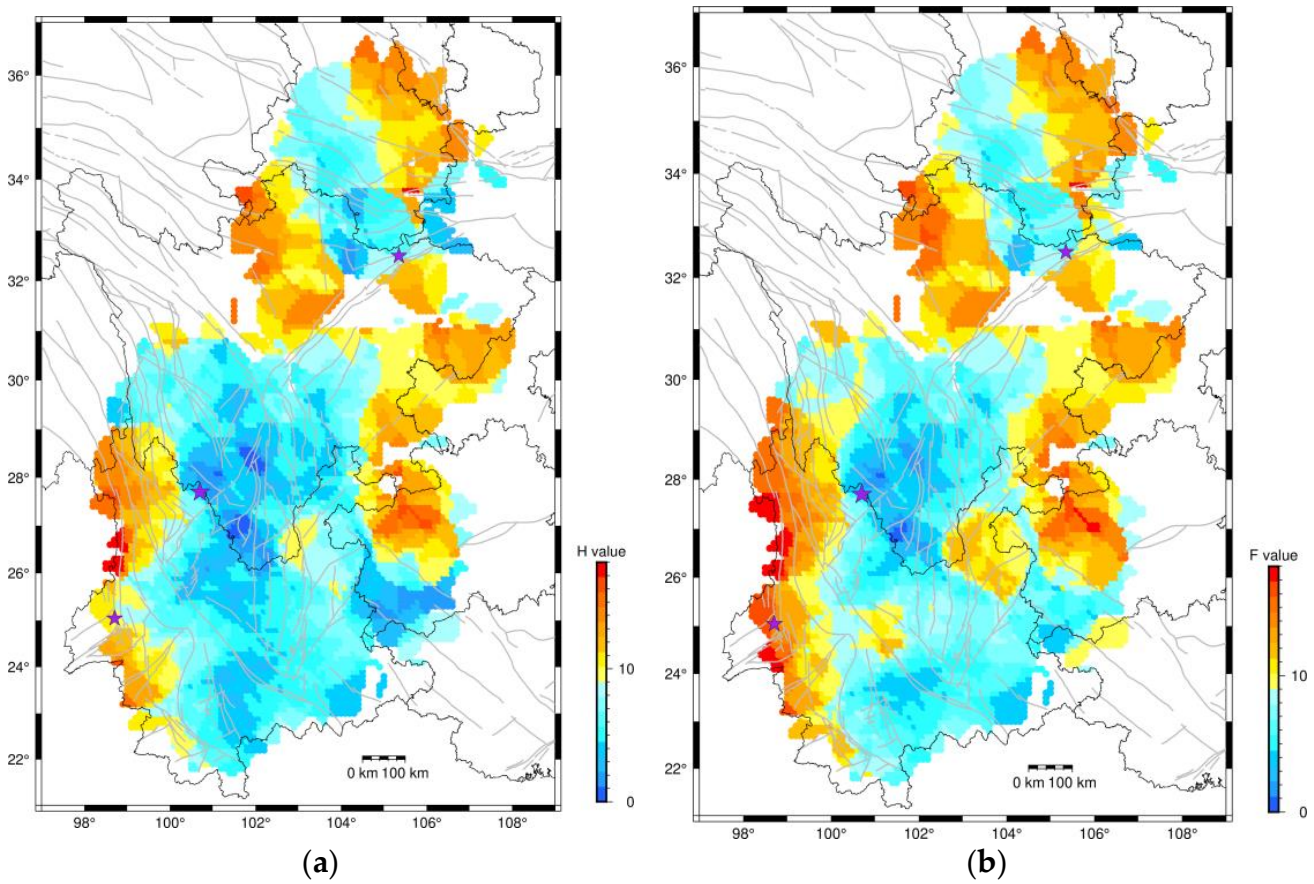

Figure 2. (**a**) Spatial distribution of H values in June 2010–June 2011. (**b**) Spatial distribution of F values in June 2010–June 2011. The purple stars show locations of events with M $\geq$ 5.0 during August 2011–July 2012. The size of the symbol is scaled to the magnitude.

Table 1. List of earthquakes in Figure 2.

Time	Longitude (°N)	Latitude (°E)	Magnitude
9 August 2011	98.7	25.0	5.2
1 November 2011	105.4	32.5	5.4
24 June 2012	100.7	27.7	5.7

The time of earthquake catalog is Beijing time.

Figure 2a,b show the spatial H value and F value during June 2010–June 2011. The lowest values of H and F are located on the border of southern Sichuan and Yunnan Province. The number of M $\geq$ 5.0 earthquake events that can be analyzed in the subsequent period is three. Among them, the largest M5.7 earthquake occurred in the areas with low H and F values.

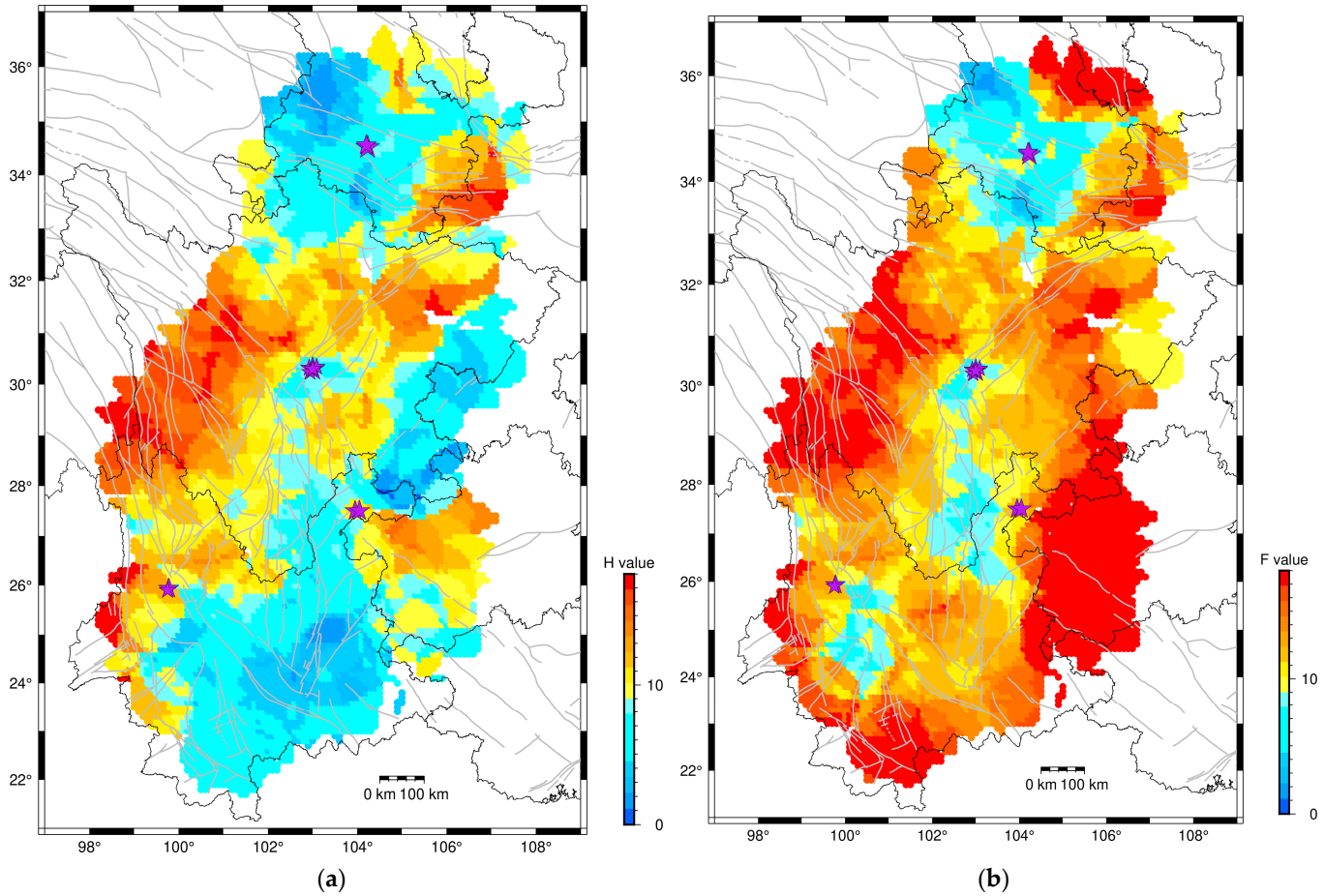

Figure 3. (**a**) Spatial distribution of *H* values in June 2011–June 2012. (**b**) Spatial distribution of *F* values in June 2011–June 2012. The purple stars show locations of events with M $\geq$ 5.0 during August 2012–July 2013. The size of the symbol is scaled to the magnitude.

Table 2. List of earthquakes in Figure 3.

Time	Longitude (°N)	Latitude (°E)	Magnitude
7 September 2012	104.0	27.5	5.7
7 September 2012	104.1	27.5	5.6
3 March 2013	99.8	25.9	5.5
17 April 2013	99.8	25.9	5.0
20 April 2013	103.0	30.3	7.0
20 April 2013	102.9	30.3	5.1
20 April 2013	102.9	30.2	5.3
21 April 2013	103.1	30.3	5.0
21 April 2013	103.0	30.3	5.4
22 July 2013	104.2	34.5	6.6
22 July 2013	104.2	34.6	5.6

The time of earthquake catalog is Beijing time.

Figure 3a,b show the spatial *H* value and *F* value during June 2011–June 2012. The distribution of *H* and *F* values is somewhat different, especially in the eastern Yunnan Province. The number of M $\geq$ 5.0 earthquake events that can be analyzed in the subsequent period is 11. These earthquakes occurred at or near the areas with low *F* values, including the M7.0 Lushan earthquake.

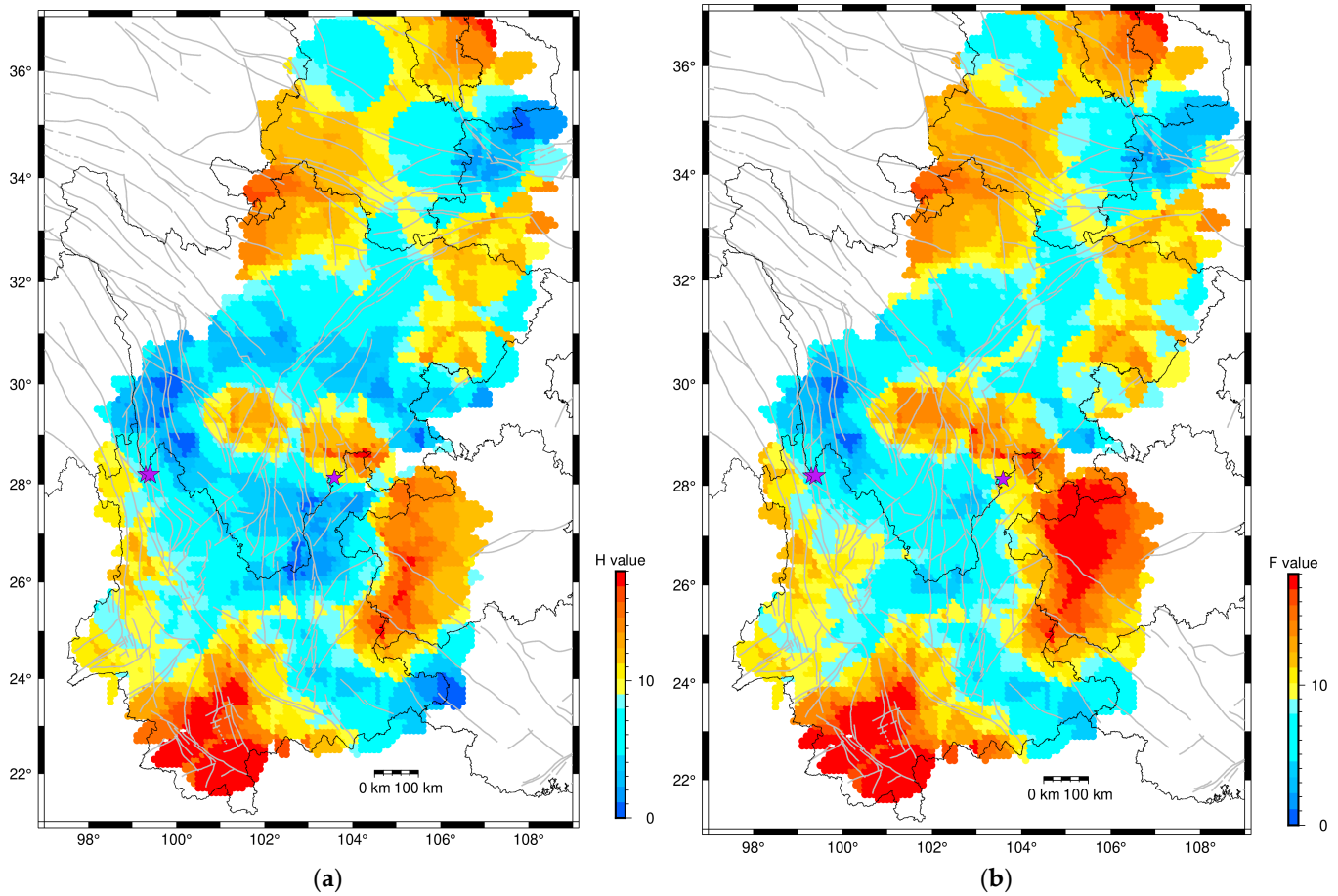

Figure 4. (**a**) Spatial distribution of *H* values in June 2012–June 2013. (**b**) Spatial distribution of *F* values in June 2012–June 2013. The purple stars show locations of events with M $\geq$ 5.0 during August 2013–July 2014.

Table 3. List of earthquakes in Figure 4.

Time	Longitude (°N)	Latitude (°E)	Magnitude
28 August 2013	99.3	28.2	5.1
31 August 2013	99.4	28.2	5.9
5 April 2014	103.6	28.1	5.3

The time of earthquake catalog is Beijing time. There are three M $\geq$ 5.0 earthquake events that are located on boundaries where the *H* and *F* value cannot be calculated, including M5.6 (97.8° N, 25° E) on 24 May 2014, M6.1 (97.8° N, 25° E), and M5.1 (97.8° N, 25° E) on 30 May 2014.

Figure 4a,b show the spatial *H* value and *F* value during June 2012–June 2013. The lowest values of *H* and *F* are located on the border of Sichuan and Yunnan Province. The number of M $\geq$ 5.0 earthquake events that can be analyzed in the subsequent period is three. They also mainly occurred near the areas with low *H* and *F* values.

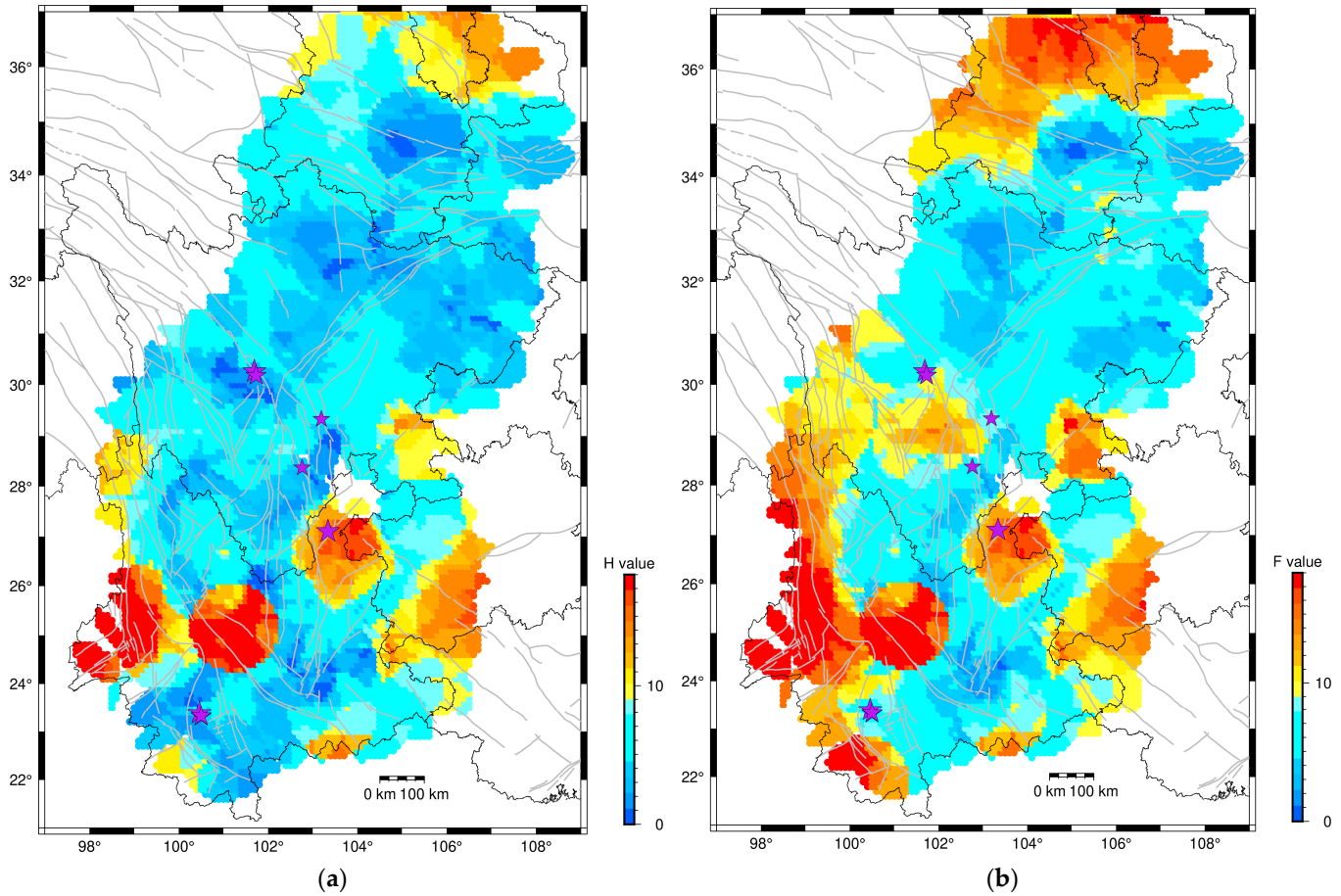

Figure 5. (**a**) Spatial distribution of *H* values in June 2013–June 2014. (**b**) Spatial distribution of *F* values in June 2013–June 2014. The purple stars show locations of events with M $\geq$ 5.0 during August 2014–July 2015.

Table 4. List of earthquakes in Figure 5.

Time	Longitude (°N)	Latitude (°E)	Magnitude
3 August 2014	103.3	27.1	6.5
1 October 2014	102.8	28.4	5.0
7 October 2014	100.5	23.4	6.6
22 November 2014	101.7	30.3	6.3
25 November 2014	101.7	30.2	5.8
6 December 2014	100.5	23.3	5.8
6 December 2014	100.5	23.3	5.9
14 January 2015	103.2	29.3	5.0

The time of earthquake catalog is Beijing time.

Figure 5a,b show the spatial *H* value and *F* value during June 2010–June 2011, respectively. The area with a low *H* value is more widely distributed than that with a low *F* value. The M $\geq$ 5.0 earthquake events in the subsequent period are mainly concentrated in south–central Sichuan and Yunnan Province. They also mainly occurred in or near the areas with low *H* and *F* values.

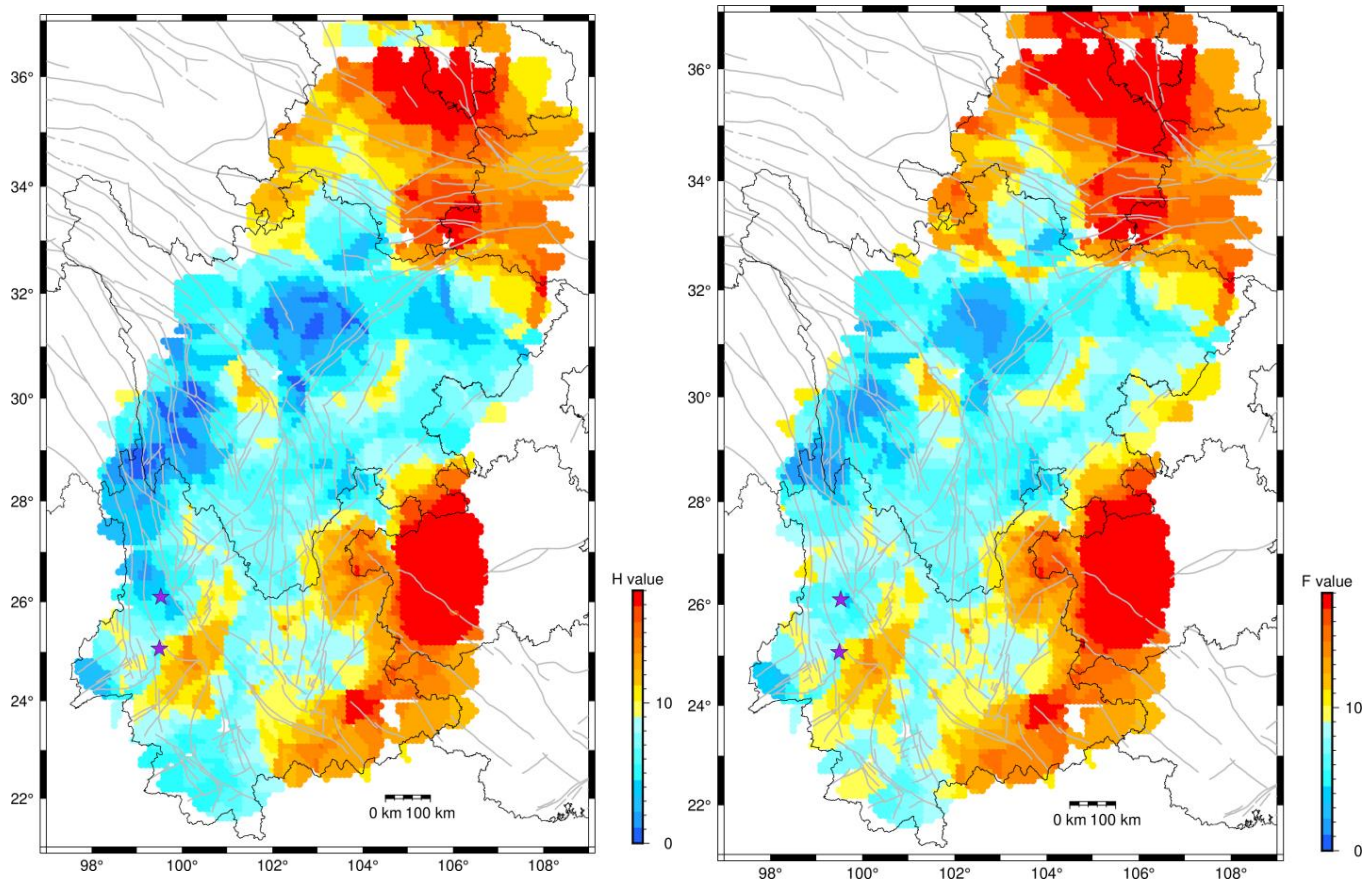

Figure 6. (**a**) Spatial distribution of *H* values in June 2014–June 2015. (**b**) Spatial distribution of *F* values in June 2014–June 2015. The purple stars show locations of events with M ≥ 5.0 during August 2015–July 2016.

Table 5. List of earthquakes in Figure 6.

Time	Longitude (°N)	Latitude (°E)	Magnitude
30 October 2015	99.5	25.1	5.1
18 May 2016	99.5	26.1	5.0

The time of earthquake catalog is Beijing time. There is one M ≥ 5.0 earthquake event (M5.0 (103.5° N, 28.1° E) on 17 August 2014) that is located on boundaries where the *H* and *F* value cannot be calculated.

Figure 6a,b show the spatial *H* value and *F* value during June 2014–June 2015. The lowest values of *H* and *F* are located in central Sichuan Province and the west border of Sichuan and Yunnan Province. In the subsequent period, two M ≥ 5.0 earthquake events occurred in the northwest Yunnan Province.

3.2. Forecasting Performance during 2010–2015

Based on the results in Section 3.1, it can be found that the spatial *H* and *F* value changes in different time periods and moderate–large earthquakes are more likely to occur in areas with low *H* and *F* values. In order to quantify the precursory information in terms of the spatial *H* and *F* value, Molchan's error diagram (MED) [30,54–56] is employed to test the forecasting performance. MED is designed for showing relationships between the rate of space tagged as predicting earthquake τ and the detection rate ν in a graph to estimate the ability of earthquake forecasting. Taking the *H* value in Figure 2a as an example, firstly, we choose a threshold of the *H* value (Hthr), and then, we alarm the grids

with an H value < Hthr in the study area. If an earthquake in the subsequent period (i.e., August 2011–July 2012) occurs in the grid with an alarm set, it is counted as a predicted event. We define N = the number of total grids with H values, N_1 = the number of grids with an alarm set, and the alarm rate can be given as $\tau = N_1/N$. We define n = the number of total events, n_1 = the number of predicted events, and the earthquake detection rate can be given as $\nu = n_1/n$. With the Hthr increasing from the minimum to maximum value in Figure 2a, the alarm rate changes. A diagonal line in the diagram indicates the prediction by the random guess (a Poisson model). Any prediction above this line indicates that the proportion of predicted earthquakes is greater than that of randomly guessed days, implying that the prediction is better than the random guess. Figure 7a,b present the MED results using the H and F values in Figures 2–6 to predict the earthquakes in each year during 2011–2016. Each symbol represents one cumulative earthquake. It is evident that the prediction rates for both H values and F values are mostly above the diagonal line, suggesting that the forecasting performance is better than a random guess. By contrast, the forecasting performance of F values is better than that of H values, since there are higher detection rates for lower alarm rates in general.

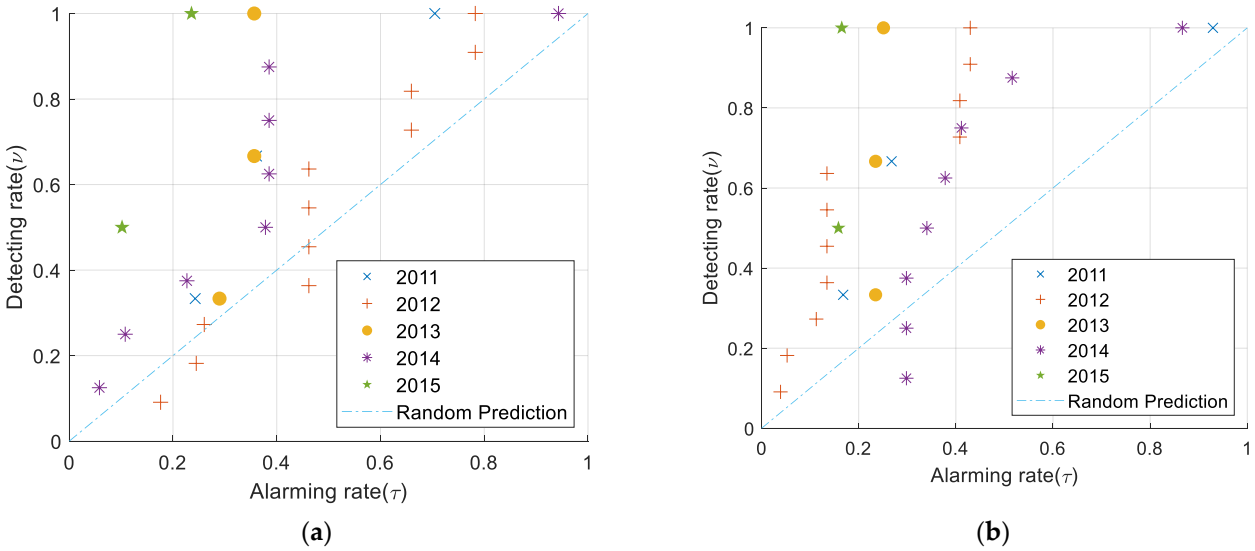

Figure 7. (**a**) MED of forecasting performance using the H values in each year. (**b**) MED of forecasting performance using the F values in each year. The different symbols show the different years' results.

To obtain comprehensive forecasting performance results during the 5 years, we set up a time–space alarm model [57] to assess it. In the model, the number of time–space cells is the total grids for each year. Since the H and F values vary from year to year, firstly, we normalize the values to 0–1 in each year. Then, we choose an alarm rate from 0 to 1, and then we alarm the cells with a normalized value < alarm rate during the 5 years. If an earthquake in the subsequent period occurs in the cell with an alarm set, it is counted as a predicted event. In the same manner as in Figure 7, we can compute the earthquake detection rate. Figure 8 shows the comprehensive forecasting performances of H and F values during August 2011–July 2016. The number of earthquake events with $M \geq 5.0$ is 27. The prediction curves of both H value and F value are above the random prediction line in Figure 8a,b. By contrast, the comprehensive forecasting performance of F values is better than that of H values, since the prediction based on H values is near the random prediction, while the prediction based on F value is clearly above the random prediction, and it exceeds the 95% confidence threshold. There are higher detection rates for lower alarm rates based on F values, and a detection rate of almost 1 can be achieved when the alarm rate is less than 0.5. Therefore, it may be better to use the total intensity of the geomagnetic field analysis, which includes the vertical component.

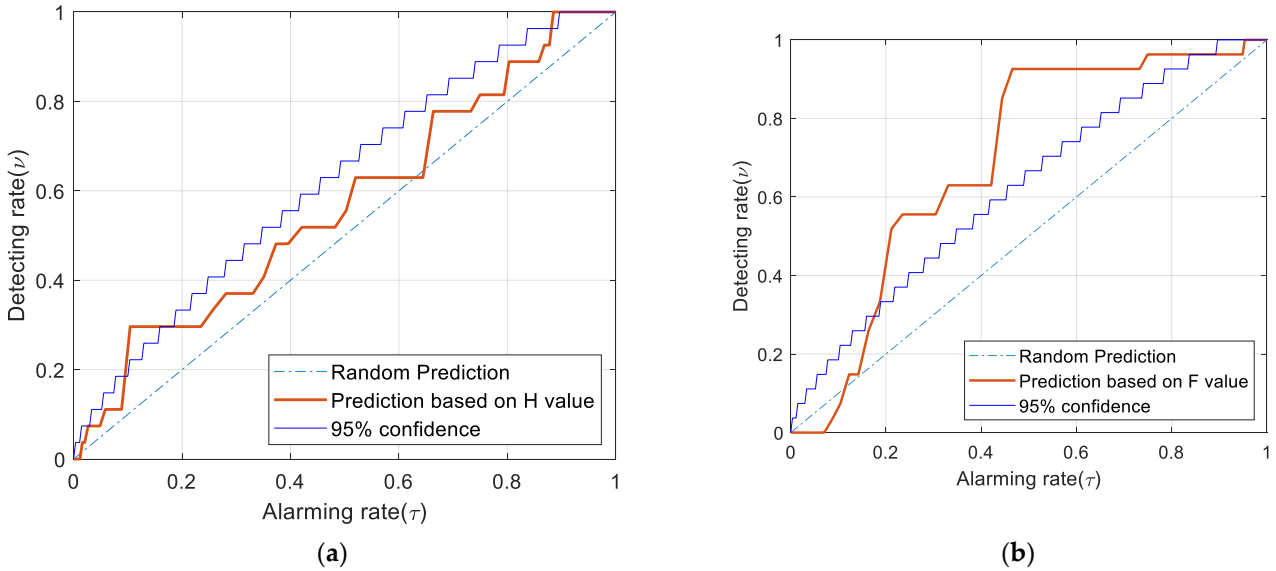

Figure 8. MED of comprehensive forecasting performance over five years. (**a**) MED of forecasting performance using the *H* values. (**b**) MED of forecasting performance using the *F* values.

4. Discussion

4.1. The Advantage of Using Mobile Geomagnetic Data When Assessing Earthquake Forecasting

The seismicity method has usually been used for inferring seismic hazards in the past [3–5]. They are usually analyzed on medium- to long-term timescales, like 5 to 10 years. Seismicity can be helpful, especially for earthquakes with foreshocks [58,59]. However, for many earthquakes, there are no foreshocks. Therefore, other geophysical observations and a comprehensive analysis must be carried out. Seismo-electromagnetic phenomena have been intensively studied during the past several decades. Although there have been reports about the anomalies of mobile geomagnetic data before earthquakes, whether it can be used as an indicator for identifying potential earthquake areas has not been explored. Thus, an assessment is absolutely essential to verify the relation between geomagnetic phenomena and large earthquakes. This paper assesses earthquake forecasting performance by using annual mobile geomagnetic observation data for the first time and proves that annual mobile geomagnetic observation data can indeed provide predictive information. The advantage of this method is that the preceding time can be shortened to one year, which is closer to the short-term analysis. In addition, previous studies have also shown the change in gravity before the M7.0 Lushan earthquake in the same region [60]. Therefore, in order to improve the forecasting performance, gravity, including horizontal gravity, seismic activity, and other physical parameters, can contribute to a comprehensive analysis. In the future, the integration of prediction information at different time scales and for different values is worth studying [24].

4.2. The Mechanism of H Value and F Value

This paper attempts to explain the reasonability of *H* value and *F* value by using the "dilatancy magnetic effect" proposed by scholars [61]. The "dilatancy magnetic effect" is inspired by the "micro-crack expansion" theory of seismic wave velocity changes in focal mechanisms. The researchers found that the local geomagnetic anomalies of earthquakes had the same duration as the wave velocity anomalies before the earthquake. There were obvious differences in the magnetic anomalies for different stations and for components' changes in the same station, reflecting the spatial changes in the magnetic anomalies. Combined with the study of rock fracture experiments and field electromagnetic sounding results, the researchers put forward the "dilatational magnetic effect" theory [61], which can produce the observed geomagnetic anomalies in the north–south seismic belt of China. The theoretical calculation of the magnetic field spatial distribution generated by the model

shows the spatial distribution characteristics as an anomalous anisotropy and symmetry of tectonic stress. As shown in Figure 9, we can see that magnetic anomalies around the earthquake are distributed in four quadrants as anomalous anisotropy and symmetry, including horizontal and vertical components. Therefore, it is reasonable that earthquakes tend to occur at low *H* and *F* values, because these two values reflect the magnetic changes in a certain range around the earthquake. If the geomagnetic stations are located In the symmetric quadrants around the earthquake center, as shown in Figure 9, the *H* value and *F* value is 0. The theories might explain the physical mechanism and reasonability of these two parameters.

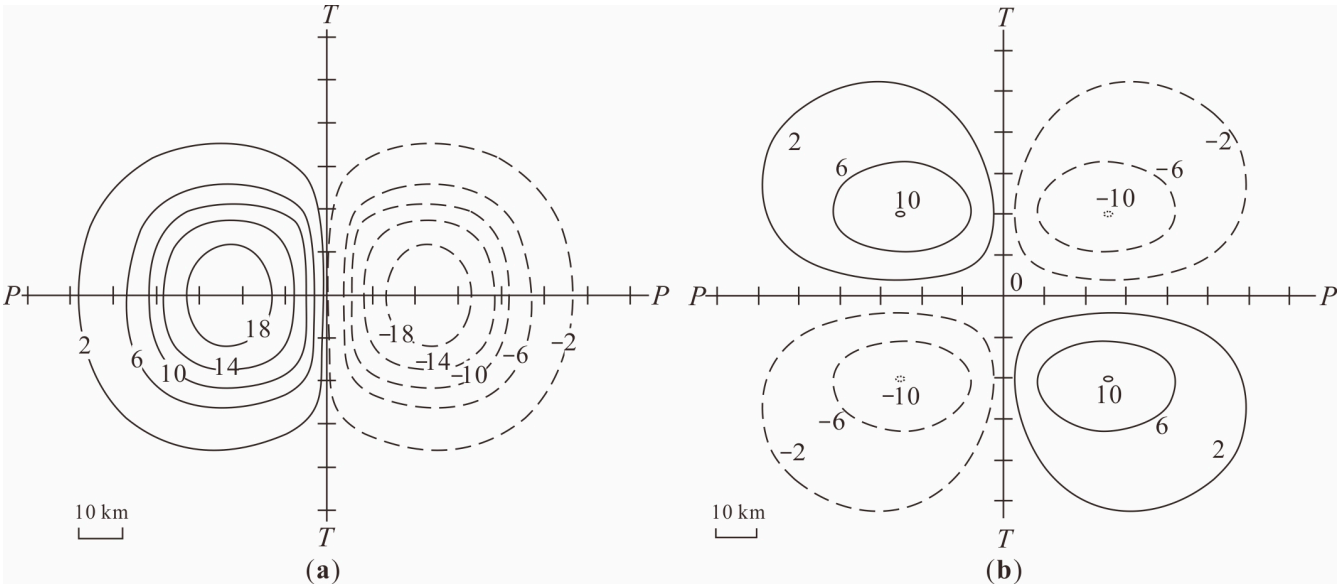

Figure 9. Theoretical calculation of the spatial distribution of the magnetic field generated by the dilatational magnetic effect model, modified from previous study [61]. The P axis is the main pressure stress axis, and the T axis is the main tensile stress axis. The center of the coordinates represents the epicenter. (**a**) Horizontal components. (**b**) Vertical components.

4.3. The Influences of Radius and Station Numbers in Parameter Selection

In Section 3, we show the *H* and *F* value results calculated for three or more stations within 100 km for each grid point. Below, we further discuss the difference in results when using different numbers of stations (Num) and distances from the center. Using the same radius of 100 km, as the Num increases, the number of grids with *H* and *F* values decreases significantly, so three is selected as the parameter of station number in this paper to avoid having too few grids. If we use other distances such as a radius of 80 km with Num $\geq$ 3, too few grid points of 80 km will also lead to insufficient data for analysis. For a radius of 150 km with Num $\geq$ 3, the grid values are sufficient, but due to the larger radius, the accuracy may not be high enough for the grids. We further discuss the MED results for Num $\geq$3 stations within 150 km, as shown in Figure 10. The prediction of both *H* values and *F* values are mostly above the diagonal line, suggesting that the forecasting performance is better than a random guess. However, compared with Figure 7, the prediction marker is much closer to the diagonal line, especially for *F* values. Figure 11 shows the forecasting performances during August 2011–July 2016. The number of earthquake events with M $\geq$ 5.0 is 31. The prediction curves of both *H* value and *F* value are above the random prediction in Figure 11a,b. It is proven that *H* and *F* values contain predictive information even if different radii are used. However, compared with Figure 7, a detection rate of almost 1 can be achieved only when the alarm rate is about 0.8, reflecting that the prediction efficiency is reduced. Therefore, the parameter selection for radius and station numbers in Section 3 exhibits a better balance between resolution and grid number in the study area.

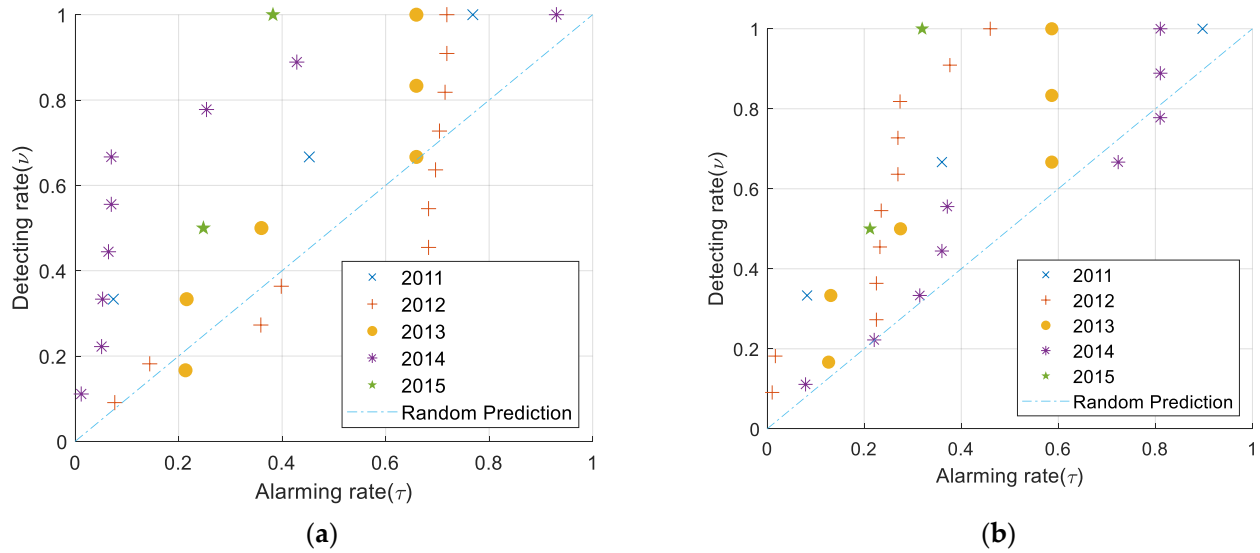

Figure 10. MED of forecasting performance in each year for Num $\geq$ 3 within 150 km. (**a**) MED of forecasting performance using the *H* values. (**b**) MED of forecasting performance using the *F* values.

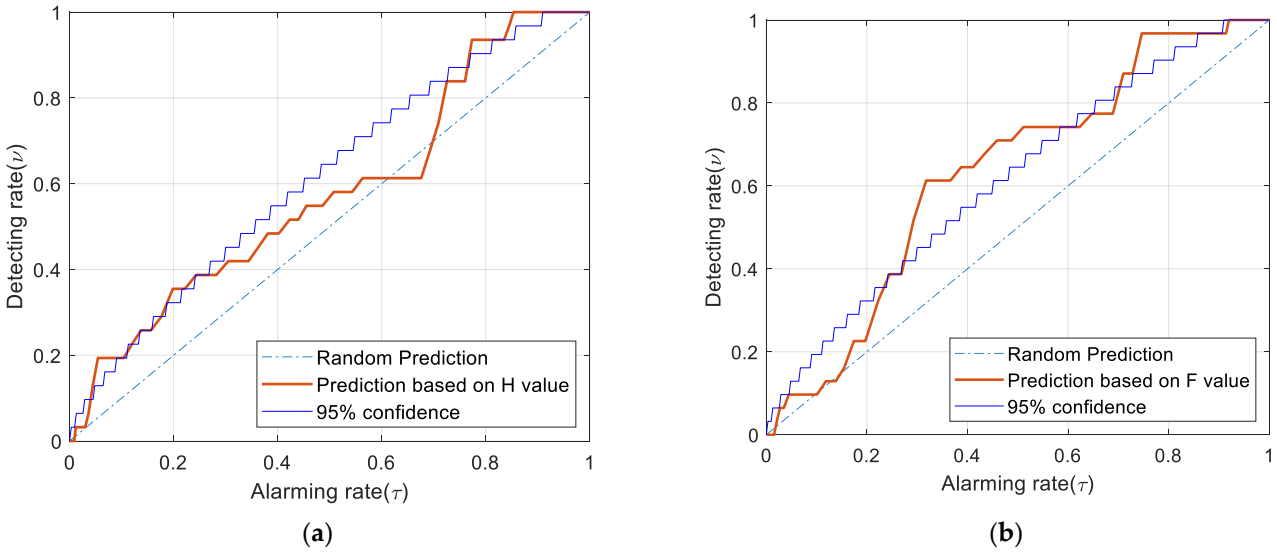

Figure 11. MED of comprehensive forecasting performance during five years for Num $\geq$ 3 within 150 km. (**a**) MED of forecasting performance using the *H* values. (**b**) MED of forecasting performance using the *F* values.

5. Conclusions

In this study, we propose two new parameters for identifying potential earthquake regions by using mobile geomagnetic observation data. The spatial *H* and *F* values are calculated in each year and then used to forecast moderate–large earthquakes (M $\geq$ 5.0) in the subsequent period. It is found that moderate–large earthquakes in southwest China are more likely to occur in low-*H* or -*F* regions. We assess their forecasting performance by using Molchan's error diagram, and the results indicate that there is considerable precursory information in the spatial *H* and *F* values. It is concluded that geomagnetic observation might be useful in middle-term earthquake forecasts in the study area. We explain the physical mechanisms that *H* and *F* values may reflect and discuss the influences of parameter selection in calculation. The methodology proposed in this study could help find the optimal solution for mobile geomagnetic measurements for middle-term earthquake forecasting.

Author Contributions: Conceptualization, Z.N. and H.C.; methodology, Z.N. and H.C.; software, H.C.; validation, Z.N., H.C., R.W., M.M., H.R., J.Y., Z.W., Y.Z. and S.Z.; formal analysis, H.C. and Z.N.; investigation, H.C., Z.N., R.W., M.M., H.R., Y.Z. and S.Z.; resources, Z.N., H.C., H.R., J.Y. and Z.W.; data curation, Z.N., Y.Z. and S.Z.; writing—original draft preparation, H.C.; writing—review and editing, Z.N., H.C., R.W., M.M., H.R., J.Y., Z.W., Y.Z. and S.Z.; visualization, Z.N. and H.C.; supervision, H.C.; project administration, Z.N. and H.C.; funding acquisition, Z.N. and H.C. All authors have read and agreed to the published version of the manuscript.

Funding: This research was supported by the National Key Research & Development Program of China (Grant No. 2023YFE0101800), the National Natural Science Foundation of China (41974083), and the Key Research and Development Plan of Yunnan Province (Grant No. 202203AC100003).

Institutional Review Board Statement: Not applicable.

Informed Consent Statement: Not applicable.

Data Availability Statement: The mobile geomagnetic data and earthquake catalog in this study are provided by Yunnan Earthquake Agency, China (https://www.yndzj.gov.cn/ accessed on 18 October 2023).

Acknowledgments: We thank Wessel et al. for the Generic Mapping Tools (GMTs) to plot some of the figures [62].

Conflicts of Interest: The authors declare no conflict of interest.

Appendix A

We design an additional description of abbreviations and/or symbols as follows: mean magnitude of resultant vector for horizontal component changes (*H* value); mean magnitude of resultant vector for three-component changes (*F* value); ultra-low frequency (ULF); very low frequency (VLF); total electron content (TEC); east component (Y); north component (X); vertical component (Z); International Association of Geomagnetism and Aeronomy (IAGA); number of stations (Num); Molchan's error diagram (MED); threshold of *H* value (Hthr); number of total grids (N); number of grids with alarm set (N_1); alarm rate (τ); number of total events (n); number of predicted events (n_1); detection rate (ν); main pressure stress axis (P axis); main tensile stress axis (T axis).

References

1. Ogata, Y. Prediction and validation of short-to-long-term earthquake probabilities in inland Japan using the hierarchical space-time ETAS and space-time Poisson process models. *Earth Planets Space* **2022**, *74*, 110. [CrossRef]
2. Iacoletti, S.; Cremen, G.; Galasso, C. Validation of the Epidemic–Type Aftershock Sequence (ETAS) Models for Simulation-Based Seismic Hazard Assessments. *Seismol. Res. Lett.* **2022**, *93*, 1601–1618. [CrossRef]
3. Wang, R.; Chang, Y.; Miao, M.; Zeng, Z.; Chen, H.; Shi, H.; Li, D.; Liu, L.; Su, Y.; Han, P. Assessing Earthquake Forecast Performance Based on b Value in Yunnan Province, China. *Entropy* **2021**, *23*, 730. [CrossRef] [PubMed]
4. Xiong, Z.; Zhou, S.; Zhuang, J. Inferring seismic hazard in Sichuan-Yunnan region of China based on the modern earthquake catalogue (1980–2019). *Earthq. Sci.* **2020**, *33*, 107–115. [CrossRef]
5. Lingfang, L.I.; Shi, Y.; Cheng, S. Exploration of long short-term memory neural network in intermediate earthquake forecast: A case study in Sichuan-Yunnan region. *Chin. J. Geophys. Chin. Ed.* **2022**, *65*, 12–25.
6. Shi, H.X.; Meng, L.Y.; Zhang, X.M.; Chang, Y.; Yang, Z.T.; Xie, W.Y.; Hattori, K.; Han, P. Decrease in b value prior to the Wenchuan earthquake (Ms8.0). *Chin. J. Geophys. Chin. Ed.* **2018**, *61*, 1874–1882.
7. Xie, W.; Hattori, K.; Han, P.; Shi, H. Temporal Variation of b Value with Statistical Test in Wenchuan Area, China Prior to the 2008 Wenchuan Earthquake. *Entropy* **2022**, *24*, 494. [CrossRef]
8. Wang, T.; Zhuang, J.; Kato, T.; Bebbington, M. Assessing the potential improvement in short-term earthquake forecasts from incorporation of GPS data. *Geophys. Res. Lett.* **2013**, *40*, 2631–2635. [CrossRef]
9. Wang, F.; Wang, M.; Wang, Y.; Shen, Z.-K. Earthquake potential of the Sichuan-Yunnan region, western China. *J. Asian Earth Sci.* **2015**, *107*, 232–243. [CrossRef]
10. Zhang, B.; Chen, S.; Zhuang, J.; Zhang, B.; Wu, X.; Liang, B. Statistical evaluation of earthquake forecast efficiency using earthquake-catalog and fault slip rate in the Sichuan-Yunnan region, China. *Front. Earth Sci.* **2023**, *11*, 1091408. [CrossRef]
11. Sarlis, N.V.; Skordas, E.S.; Christopoulos, S.-R.G.; Varotsos, P.A. Natural Time Analysis: The Area under the Receiver Operating Characteristic Curve of the Order Parameter Fluctuations Minima Preceding Major Earthquakes. *Entropy* **2020**, *22*, 583. [CrossRef] [PubMed]

12. Liu, J.-Y.; Hattori, K.; Chen, Y.-I. Application of Total Electron Content Derived from the Global Navigation Satellite System for Detecting Earthquake Precursors. In *Pre–Earthquake Processes*; Ouzounov, D., Pulinets, S., Hattori, K., Taylor, P., Eds.; American Geophysical Union: Washington, DC, USA, 2018; pp. 305–317.
13. Zhang, X.M.; Shen, X.H. The development in seismo-ionospheric coupling mechanism. *Prog. Earthq. Sci. Chin. Ed.* **2022**, *52*, 193–202.
14. Han, P.; Zhuang, J.; Hattori, K.; Chen, C.-H.; Febriani, F.; Chen, H.; Yoshino, C.; Yoshida, S. Assessing the Potential Earthquake Precursory Information in ULF Magnetic Data Recorded in Kanto, Japan during 2000–2010: Distance and Magnitude Dependences. *Entropy* **2020**, *22*, 859. [CrossRef] [PubMed]
15. Uyeda, S.; Nagao, T.; Kamogawa, M. Short-term earthquake prediction: Current status of seismo-electromagnetics. *Tectonophysics* **2009**, *470*, 205–213. [CrossRef]
16. Hattori, K. ULF Geomagnetic Changes Associated with Large Earthquakes. *Terr. Atmos. Ocean. Sci.* **2004**, *15*, 329–360. [CrossRef]
17. Han, P.; Hattori, K.; Hirokawa, M.; Zhuang, J.; Chen, C.; Febriani, F.; Yamaguchi, H.; Yoshino, C.; Liu, J.; Yoshida, S. Statistical analysis of ULF seismomagnetic phenomena at Kakioka, Japan, during 2001–2010. *J. Geophys. Res.* **2014**, *119*, 4998–5011. [CrossRef]
18. Huang, Q.; Han, P.; Hattori, K.; Ren, H. Electromagnetic Signals Associated with Earthquakes. In *Seismoelectric Exploration*; Grobbe, N., Revil, A., Zhu, Z., Slob, E., Eds.; American Geophysical Union: Washington, DC, USA, 2020; pp. 415–436.
19. Liu, X.; Hattori, K.; Han, P.; Chen, H.; Chie, Y.; Zhao, X. Possible Anomalous Changes in Solar Quiet Daily Geomagnetic Variation (Sq) Related to the 2011 off the Pacific coast of Tohoku Earthquake (Mw 9.0). *Pure Appl. Geophys.* **2020**, *177*, 333–346. [CrossRef]
20. Chen, C.-H.; Sun, Y.-Y.; Lin, K.; Zhou, C.; Xu, R.; Qing, H.; Gao, Y.; Chen, T.; Wang, F.; Yu, H.; et al. A New Instrumental Array in Sichuan, China, to Monitor Vibrations and Perturbations of the Lithosphere, Atmosphere, and Ionosphere. *Surv. Geophys.* **2021**, *42*, 1425–1442. [CrossRef]
21. Febriani, F.; Dewi, C.N.; Ahadi, S.; Anggono, T.; Syuhada; Hasib, M.; Prasetio, A.D. Detrended Fluctuation Analysis (DFA) of Gunungsitoli Geomagnetic Station to Assess the Possibility of the Earthquake Precursor. In Proceedings of the International Conference on Radioscience, Equatorial Atmospheric Science and Environment and Humanosphere Science, Singapore, 3 July 2023; Basit, A., Yulihastin, E., Cahyarini, S.Y., Santoso, H., Pranowo, W.S., Slamet, S.L., Belgaman, H.A., Eds.; Springer Nature: Singapore, 2023; pp. 45–54.
22. Febriani, F.; Han, P.; Yoshino, C.; Hattori, K.; Nurdiyanto, B.; Effendi, N.; Maulana, I.; Gaffar, E. Ultra low frequency (ULF) electromagnetic anomalies associated with large earthquakes in Java Island, Indonesia by using wavelet transform and detrended fluctuation analysis. *Nat. Hazards Earth Syst. Sci.* **2014**, *14*, 789–798. [CrossRef]
23. Ouzounov, D.; Pulinets, S.; Hattori, K.; Taylor, P. *Pre-Earthquake Processes: A Multidisciplinary Approach to Earthquake Prediction Studies*; John Wiley & Sons: Hoboken, NJ, USA, 2018; Volume 234.
24. Chen, H.; Han, P.; Hattori, K. Recent Advances and Challenges in the Seismo-Electromagnetic Study: A Brief Review. *Remote Sens.* **2022**, *14*, 5893. [CrossRef]
25. Han, P.; Huang, Q.H.; Xiu, J.G. Principal component analysis of geomagnetic diurnal variation associated with earthquakes: Case study of the M6.1 Iwate-ken Nairiku Hokubu earthquake. *Chin. J. Geophys. Chin. Ed.* **2009**, *52*, 1556–1563.
26. Zhang, X.; Li, M.; Guan, H.P. Anomaly analysis of earth resistivity observations before the Wenchuan earthquake. *Earthquake* **2009**, *29*, 108–115.
27. Xie, T.; Xue, Y.; Ye, Q.; Lu, J. Anisotropic change in apparent resistivity before earthquakes of MS $\geq$ 7.0 in China mainland. *Geomat. Nat. Hazards Risk* **2022**, *13*, 1207–1228. [CrossRef]
28. Wang, T.; Cui, B.; Ye, Q.; Li, J.; Wang, L.; Tong, Q. Temporal-spatial distribution of apparent resistivity before and after the Jiuzhaigou Ms7.0 earthquake. *Chin. J. Geophys. Chin. Ed.* **2020**, *63*, 2345–2356.
29. Ouyang, X.Y.; Parrot, M.; Bortnik, J. ULF Wave Activity Observed in the Nighttime Ionosphere Above and Some Hours Before Strong Earthquakes. *J. Geophys. Res. Space Phys* **2020**, *125*, e2020JA028396. [CrossRef]
30. Han, P.; Hattori, K.; Zhuang, J.; Chen, C.; Liu, J.; Yoshida, S. Evaluation of ULF seismo-magnetic phenomena in Kakioka, Japan by using Molchan's error diagram. *Geophys. J. Int.* **2017**, *208*, 482–490. [CrossRef]
31. Han, P.; Hattori, K.; Huang, Q.; Hirano, T.; Ishiguro, Y.; Yoshino, C.; Febriani, F. Evaluation of ULF electromagnetic phenomena associated with the 2000 Izu Islands earthquake swarm by wavelet transform analysis. *Nat. Hazards Earth Syst. Sci.* **2011**, *11*, 965–970. [CrossRef]
32. Hattori, K.; Han, P. Statistical analysis and assessment of ultralow frequency magnetic signals in Japan as potential earthquake precursors. In *Pre-Earthquake Processes: A Multidisciplinary Approach to Earthquake Prediction Studies*; John Wiley & Sons: Hoboken, NJ, USA, 2018; p. 229.
33. Hattori, K.; Han, P.; Yoshino, C.; Febriani, F.; Yamaguchi, H.; Chen, C. Investigation of ULF Seismo-Magnetic Phenomena in Kanto, Japan During 2000–2010: Case Studies and Statistical Studies. *Surv. Geophys.* **2013**, *34*, 293–316. [CrossRef]
34. Politis, D.; Potirakis, S.M.; Hayakawa, M. Criticality analysis of 3-year-long VLF subionospheric propagation data possibly related to significant earthquake events in Japan. *Nat. Hazards* **2020**, *102*, 47–66. [CrossRef]
35. Shen, X.H.; Zhima, Z.R.; Zhao, S.F.; Qian, G.; Ye, Q.; Ruzhin, Y. VLF radio wave anomalies associated with the 2010 Ms 7.1 Yushu earthquake. *Adv. Space Res.* **2017**, *59*, 2636–2644. [CrossRef]

36. Maurya, A.K.; Venkatesham, K.; Tiwari, P.; Vijaykumar, K.; Singh, R.; Singh, A.K.; Ramesh, D.S. The 25 April 2015 Nepal Earthquake: Investigation of precursor in VLF subionospheric signal. *J. Geophys. Res. Space Phys.* **2016**, *121*, 10403–10416. [CrossRef]
37. Popova, I.; Rozhnoi, A.; Solovieva, M.; Chebrov, D.; Hayakawa, M. The Behavior of VLF/LF Variations Associated with Geomagnetic Activity, Earthquakes, and the Quiet Condition Using a Neural Network Approach. *Entropy* **2018**, *20*, 691. [CrossRef] [PubMed]
38. Heki, K. Ionospheric electron enhancement preceding the 2011 Tohoku-Oki earthquake. *Geophys. Res. Lett.* **2011**, *38*, 6011–6015. [CrossRef]
39. He, L.M.; Heki, K. Three-dimensional distribution of ionospheric anomalies prior to three large earthquakes in Chile. *Geophys. Res. Lett.* **2016**, *43*, 7287–7293. [CrossRef]
40. Iwata, T.; Umeno, K. Preseismic ionospheric anomalies detected before the 2016 Kumamoto earthquake. *J. Geophys. Res. Space Phys.* **2017**, *122*, 3602–3616. [CrossRef]
41. Chen, H.; Miao, M.; Chang, Y.; Wang, Q.; Shen, X.; Hattori, K.; Han, P. Singular Spectrum Analysis of the Total Electron Content Changes Prior to M $\geq$ 6.0 Earthquakes in the Chinese Mainland During 1998–2013. *Front. Earth Sci.* **2021**, *9*, 677163. [CrossRef]
42. Wang, Z.; Su, S.; Yuan, J. The existence of underground gas storage causes geomagnetic anomaly in this area? *J. Phys. Conf. Ser.* **2021**, *1980*, 012007. [CrossRef]
43. Wang, Z.; Yuan, J.; Chen, B.; Chen, S.; Wang, C.; Mao, F. Local magnetic field changes during gas injection and extraction in an underground gas storage. *Geophys. J. Int.* **2019**, *217*, 271–279. [CrossRef]
44. Wang, Z.; Chen, B.; Yuan, J.; Yang, F.; Jia, L.; Wang, C. Localized geomagnetic field anomalies in an underground gas storage. *Phys. Earth Planet. Inter.* **2018**, *283*, 92–97. [CrossRef]
45. Gu, Z.; Zhan, Z.; Gao, J.; Han, W.; An, Z.; Yao, T.; Chen, B. Geomagnetic survey and geomagnetic model research in China. *Earth Planets Space* **2006**, *58*, 741–750. [CrossRef]
46. Pushkov, A.; Fainberg, E.; Chernova, T.; Fiskina, M. Analysis of the space-time structure of the main geomagnetic field by expansion into natural orthogonal component. *Geomagn. Aeron.* **1976**, *16*, 337–343.
47. Xu, W.Y.; Sun, W. Eigen mode analysis of earth's main magnetic field. *Acta Geophys. Sin. Chin. Ed.* **1998**, *41*, 2002.
48. Xu, W.Y. NOC model of the earth's main magnetic field. *Chin. J. Geophys. Chin. Ed.* **2002**, *32*, 576–587. [CrossRef]
49. Gu, Z.W.; Chen, B.; Gao, J.T.; Xin, C.J.; Yuan, H.H.; Di, C.Z. Research of geomagnetic spatial-temporal variations in China by NOC method. *Chin. J. Geophys. Chin. Ed.* **2009**, *52*, 2602–2612.
50. Alken, P.; Maus, S.; Chulliat, A.; Manoj, C. NOAA/NGDC candidate models for the 12th generation International Geomagnetic Reference Field. *Earth Planets Space* **2015**, *67*, 68. [CrossRef]
51. Ni, Z.; Chen, S.G.; Yuan, H.H.; Yi, W.; Wang, C. Research on Anomalies Variation of Lithosphere Magnetic Field Before and After Lushan Ms7. 0 Earthquake. *J. Seismol. Res. Chin. Ed.* **2014**, *37*, 61–65.
52. Ni, Z. Analysis of Anomalous Characteristics of Geomagnetic Change before and after Eryuan M5. 5 Earthquake. *J. Seismol. Res. Chin. Ed.* **2014**, *37*, 426–432.
53. Ni, Z.; Yuan, H.H.; Wang, C.; Chen, S.G.; Yan, W.S. Analysis of Local Anomalous Characteristics of Lithospheric Magnetic Field before Ludian M6. 5 and Yongshan M5. 0 Earthquakes in Yunnan in 2014. *J. Seismol. Res. Chin. Ed.* **2014**, *37*, 537–541.
54. Molchan, G.M. Structure of optimal strategies in earthquake prediction. *Tectonophysics* **1991**, *193*, 267–276. [CrossRef]
55. Molchan, G.M. Earthquake prediction as a decision-making problem. *Pure Appl. Geophys.* **1997**, *149*, 233–247. [CrossRef]
56. Molchan, G.M. Strategies in strong earthquake prediction. *Phys. Earth Planet. Inter.* **1990**, *61*, 84–98. [CrossRef]
57. Molchan, G. Space—Time Earthquake Prediction: The Error Diagrams. In *Seismogenesis and Earthquake Forecasting: The Frank Evison Volume II*; Savage, M.K., Rhoades, D.A., Smith, E.G.C., Gerstenberger, M.C., Vere-Jones, D., Eds.; Springer: Basel, Switzerland, 2010; pp. 53–63.
58. Zhu, G.; Yang, H.; Tan, Y.J.; Jin, M.; Li, X.; Yang, W. The cascading foreshock sequence of the Ms 6.4 Yangbi earthquake in Yunnan, China. *Earth Planet. Sci. Lett.* **2022**, *591*, 117594. [CrossRef]
59. Wang, R.; Chang, Y.; Han, P.; Miao, M.; Zhiyi, Z.; Shi, H.; Li, D.; Liu, L.; Su, Y. Optimized Traffic Light System with AIC and Application to the 2021 M6.7 Yangbi Earthquake Sequence. *Entropy* **2023**, *25*, 759. [CrossRef] [PubMed]
60. Wang, L.; Chen, S.; Zhuang, J.; Zhang, B.; Shi, W.; Yang, J.; Xu, W. Gravity field changes reveal deep mass transfer before and after the 2013 Lushan earthquake. *Commun. Earth Environ.* **2023**, *4*, 194. [CrossRef]
61. Qi, G.Z. On the dilatancy-magnetic effect. *Acta Geophys. Sin. Chin. Ed.* **1978**, *21*, 18–33.
62. Wessel, P.; Luis, J.F.; Uieda, L.; Scharroo, R.; Wobbe, F.; Smith, W.H.F.; Tian, D. The Generic Mapping Tools Version. *Geochem. Geophys. Geosystems* **2019**, *20*, 5556–5564. [CrossRef]